EUROPEAN ORGANIZATION FOR NUCLEAR RESEARCH (CERN)

Improved performance of the LHCb Outer Tracker in LHC Run 2

The LHCb Outer Tracker group

Ph. d'Argent[1], L. Dufour[2], L. Grillo[7], J.A. de Vries[2], A. Ukleja[6], R. Aaij[8], F. Archilli[2], S. Bachmann[1], D. Berninghoff[1], A. Birnkraut[3], J. Blouw[9†], M. De Cian[1], G. Ciezarek[2], Ch. Färber[1], M. Demmer[3], F. Dettori[4], E. Gersabeck[1], J. Grabowski[1], W.D. Hulsbergen[2], B. Khanji[1], M. Kolpin[1], M. Kucharczyk[5], B.P. Malecki[5], M. Merk[2], M. Mulder[2], J. Müller[3], V. Mueller[3], A. Pellegrino[2], M. Pikies[5], B. Rachwal[11], T. Schmelzer[3], B. Spaan[3], M. Szczekowski[6], J. van Tilburg[2], S. Tolk[10], N. Tuning[2], U. Uwer[1], J. Wishahi[3], M. Witek[5],

[1]Physikalisches Institut, Heidelberg, Germany
[2]Nikhef, Amsterdam, The Netherlands
[3]Technische Universität Dortmund, Germany
[4]Oliver Lodge Laboratory, University of Liverpool, Liverpool, United Kingdom
[5]H. Niewodniczanski Institute of Nuclear Physics, Cracow, Poland
[6]National Center for Nuclear Research (NCBJ), Warsaw, Poland
[7]Bicocca University, Milano, Italy
[8]European Organization for Nuclear Research (CERN), Geneva, Switzerland
[9]Max Planck-Institut Für Kernphysik (MPIK), Heidelberg, Germany
[10]Cavendish Laboratory, University of Cambridge, Cambridge, United Kingdom
[11]AGH - University of Science and Technology, Faculty of Physics and Applied Computer Science, Krakow, Poland
† Deceased

Abstract

The LHCb Outer Tracker is a gaseous detector covering an area of $5 \times 6\,\text{m}^2$ with 12 double layers of straw tubes. The performance of the detector is presented based on data of the LHC Run 2 running period from 2015 and 2016. Occupancies and operational experience for data collected in pp, pPb and PbPb collisions are described. An updated study of the ageing effects is presented showing no signs of gain deterioration or other radiation damage effects. In addition several improvements with respect to LHC Run 1 data taking are introduced. A novel real-time calibration of the time-alignment of the detector and the alignment of the single monolayers composing detector modules are presented, improving the drift-time and position resolution of the detector by 20%. Finally, a potential use of the improved resolution for the timing of charged tracks is described, showing the possibility to identify low-momentum hadrons with their time-of-flight.

arXiv:1708.00819v2 [physics.ins-det] 2 Feb 2018

Contents

1   Introduction

The LHCb experiment is dedicated to the study of *CP* violation and rare decays of hadrons with *b* and *c* quarks at the Large Hadron Collider. The LHCb detector [1] is a single arm forward spectrometer, with an acceptance in the pseudorapidity range $2 < \eta < 5$. The tracking system of the detector is composed of a silicon-strip vertex detector, close to the proton-proton interaction region, and five tracking stations: two upstream and three downstream of a dipole magnet with bending power of around 4 Tm. The upstream tracking stations and the inner part of the downstream ones are composed of silicon-strip detectors. The outer part of the downstream stations is covered by the Outer Tracker (OT) [2], a straw-tube gaseous detector. The single hit resolution in the OT leads to a momentum resolution of $\delta p/p \approx 0.4\%$, providing a superior mass resolution of reconstructed charm and bottom decays.

The OT covers an area of about $5 \times 6\,\mathrm{m}^2$ starting from a minimum distance of about 10 cm from the beam direction. The cross-shaped inner region not covered by the OT, $|y| < 10\,\mathrm{cm}$ for $|x| < 59.7\,\mathrm{cm}$, and $|y| < 20\,\mathrm{cm}$ for $|x| < 25.6\,\mathrm{cm}$, is instrumented with silicon strip detectors [1].[1] Each straw tube measures the drift time of charges created by the ionising particles, and collected on the anode wire. The straw tubes are 2.4 m long with 4.9 mm inner diameter. The anode wire at the straw centre is set to $+1550\,\mathrm{V}$ and is made of $25\,\mu\mathrm{m}$ thick gold plated tungsten. The cathode consists of a $40\,\mu\mathrm{m}$ thick inner foil of electrically conducting carbon doped Kapton-XC [2] and a $25\,\mu\mathrm{m}$ thick outer foil, consisting of Kapton-XC laminated together with a $12.5\,\mu\mathrm{m}$ thick layer of aluminium. The straws are arranged in modules in two staggered layers glued to sandwich panels, using Araldite AY103-1.[3] Two panels are sealed with $400\,\mu\mathrm{m}$ thick carbon fibre sidewalls, resulting in a gas-tight box enclosing a stand-alone detector module. The straws are filled with a gas mixture of $\mathrm{Ar}/\mathrm{CO}_2/\mathrm{O}_2$ (70/28.5/1.5) which guarantees a fast drift time below 50 ns. The gas in input to the modules has an overpressure of 2.5 mbar. The modules are composed of two staggered layers (monolayers) of 64 drift tubes each. A cross-section of the module layout is shown in figure 1(a).

Two types of modules are used: type *F* modules, which have an active length of 4850 mm, have monolayers split in the middle into two independent readout sections read out from the outer ends; type *S* modules have about half the length of *F*-type modules, they are mounted above and below the beampipe, and are read out from the outer module end. One detector layer is built from 14 long and 8 short modules, see figure 1(b). The complete OT detector consists of 168 long and 96 short modules and comprises 53,760 single straw-tube channels.

The detector modules are arranged in three stations. Each station consists of four module layers, arranged in an *x-u-v-x* geometry: the modules in the *x*-layers are oriented

---

[1]The LHCb coordinate system is a right-handed coordinate system, with the z axis pointing along the beam axis, y the vertical direction, and x the horizontal direction. The (x, z) plane is the bending plane of the dipole magnet.

[2]Kapton® is a polyimide film developed by DuPont.

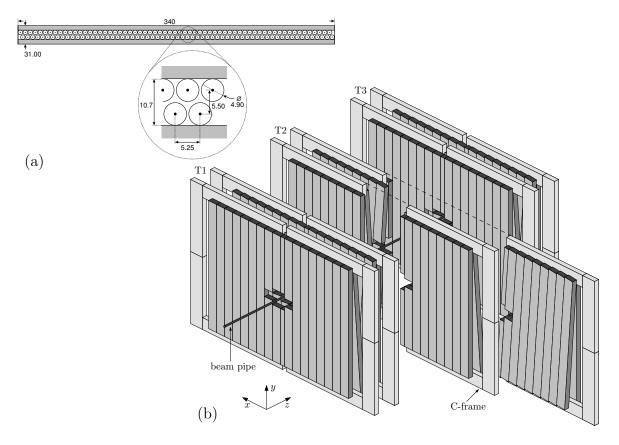[3]Araldite® is a two component epoxy resin developed by Huntsman.

Figure 1: (a) OT module cross section, with distances in mm. (b) Arrangement of OT straw-tube modules in layers and stations.

vertically, whereas those in the u and v layers are tilted by $+5^o$ and -5° with respect to the vertical, respectively. This leads to a total of 24 straw layers positioned along the z-axis.

Each station is split into two halves, retractable on both sides of the beam line. Each half consists of two independently movable units, known as C-frames, see figure 1(b). The modules are positioned on the C-frames by means of precision dowel pins. The C-frames also provide routing for all detector services (gas, low and high voltage, cooling water, data fibres, slow and fast control). The C-frames are sustained by a stainless steel structure (called "bridge"), equipped with rails allowing the independent movement of all twelve C-frames. The bridge is mounted on a concrete structure (called "table").

The front-end (FE) electronics measures the arrival times of the ionization clusters produced by charged particles traversing the straw-tubes with respect to the beam crossing (BX) signal [3]. The signals are amplified and subsequently discriminated against a threshold value. This value is set as low as possible to minimize the effect of time-walk on the drift time resolution, and at the same time to keep the number of noise hits at an acceptable level. The measured arrival times are then digitized for each 25 ns (the LHC design value for the minimum bunch crossing interval) and stored in a digital pipeline to

await the lowest-level trigger (L0) decision. This TDC value is given in units of 0.4 ns, as the 25 ns window is encoded with 6 bits. On a positive L0 decision, the digitized data of the triggered bunch crossing and of the following two bunch crossings (for a total window of 75 ns) are transmitted via optical links to TELL1 boards in the LHCb DAQ system [4].

The performance of the OT as studied in detail during Run 1 of LHC (data-taking years 2009-2012) can be found in Ref. [5], together with additional details of the apparatus.

Thanks to improvements on the LHC magnets during the Long Shutdown 1 (LS1) period in 2013 and 2014, the LHC provided collisions at a higher centre-of-mass energy of 13 TeV in Run 2 (versus 7 and 8 TeV in Run 1) and proton bunches with a time spacing of 25 ns instead of 50 ns. While these conditions are closer to the design values, they are novel, challenging circumstances, motivating the documentation of the performance of the detector in this paper.

This paper describes the detector performance and improvements in the LHC Run 2 period with data collected in 2015 and 2016. In the first part, the performance with proton-proton (pp) and lead-lead (PbPb) collisions are discussed in section 2. In section 3 a study is presented of the mechanical stability of the OT obtained through a hardware alignment system (called "RASNIK"). In section 4 an updated study of the ageing of the detector is reported.

Furthermore several improvements to the OT were carried out during LS1 and are presented in the second part. Owing to an improved online event filter farm, the two levels of the LHCb High Level Trigger (HLT) were split in two stages, allowing for a full real-time alignment and calibration of the whole detector used by the second stage of the online event selection [6]. In section 5 a novel real-time calibration of the global time alignment of the OT with respect to the LHC clock is presented, while in section 6 the single front-end alignment and calibration is discussed. An updated calibration of the distance drift-time relation is reported in section 7. The drift-time measurement capabilities of the OT have been used to measure the time of flight of tracks, which can be exploited for particle identification and for primary interaction vertex assignment and distinction. This method was developed and used for the first time in Run 2, and is presented in section 8 together with its performance.

Part I
Operational experience

The monitoring and evaluation of the detector performance is crucial to maintain the same quality data needed for the physics measurements as in Run 1. In this first part of the paper, the performance and stability of the detector operation is presented, together with studies on possible radiation damage due to the received dose.

2 Event occupancies in proton and lead collisions

2.1 Performance in Run 2 pp collisions

The performance of the Outer Tracker in Run 1 exceeded expectations in terms of low number of dead and noisy channels, single hit resolution, and tracking performance, and has been extensively described elsewhere [5].

The larger center-of-mass energy and the increased spill-over due to the 25 ns bunch spacing lead to a larger OT occupancy. In order to keep the OT event multiplicity at a similar level with respect to Run 1, to maintain the same performance of the track reconstruction, the average number of overlapping events per bunch crossing was reduced from $\mu = 1.7$ in Run 1, to $\mu = 1.1$ in Run 2. The resulting distributions of the OT event occupancies are compared in figure 2(a). Due to the fact that the event occupancy in Run 2 is the result of adding the occupancies of multiple bunch crossings, the final event occupancy has a smaller spread. In 2017 the OT hit occupancy was further reduced by limiting the number of spill-over hits from the previous bunch crossing (see section 2.2).
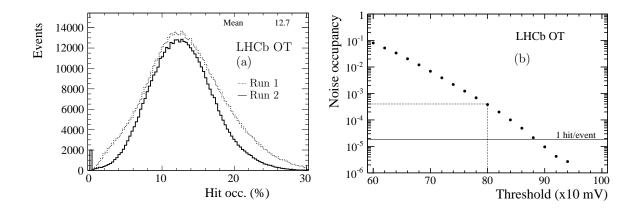
Figure 2: (a) Event occupancy for the OT in Run 1 (dottet line) and Run 2 (solid line). The event occupancy in the OT is on average 13% in Run 2. (b) Occupancy of noise hits as a function of the discriminator threshold.
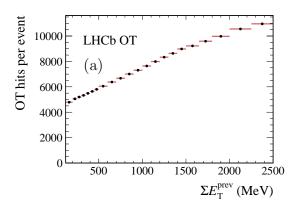
The fraction of noise hits that contribute to the event occupancy is negligible. With the nominal discriminator threshold of 800 mV, about 30 noise hits are expected every event, as shown in figure 2(b). As far as dead channels are concerned, only 8 out of a total of 53760 straws do not give any signal, as they had to be disconnected to avoid large currents due to short-circuits.

2.2   Occupancies and hits from previous bunch crossings

The OT readout window contains three consecutive bunch crossings of 25 ns upon each L0 trigger, to ensure that late hits with long drift-times are also recorded. Similarly, late hits from the previous bunch crossing will be recorded in the OT as early hits from the triggered bunch crossing. These so-called spill-over hits hamper the track reconstruction, enlarging the fraction of fake tracks. In addition, these hits from the previous spill consume bandwidth in the data transmission.

The scalar sum of the transverse energy of all hadronic calorimeter clusters of the previous bunch crossing, $\Sigma E_T^{\mathrm{Prev}}$, is available in the L0 trigger decision unit. To quantify the influence of spill-over on the tracker's performance, the occupancy and drift times of no-bias events are analysed in bins of the scalar sum of transverse energy of all hadronic calorimeter clusters in the previous bunch crossing. The average number of hits recorded as a function of $\Sigma E_T^{\mathrm{Prev}}$ is shown in figure 3(a). It can be seen that the occupancy in the OT is double for events with a very busy previous event, $\Sigma E_T^{\mathrm{Prev}} \approx 2000 (= 48\,\mathrm{GeV})$.

This feature will be used in 2017 by selecting events with $\Sigma E_T^{\mathrm{Prev}} < 1000 (= 24\,\mathrm{GeV})$, which rejects 7.2% of the events (figure 3(b)). This does not bias the topology of the physical event because the event multiplicity in the calorimeter is not correlated between consecutive bunch crossings. The effect on the drift time spectrum is illustrated in figure 4(a). As expected the largest effect of this cut is on the number of (fake) early hits,
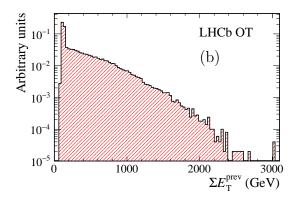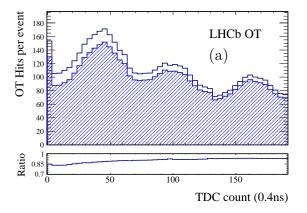

Figure 3: (a) The average number of recorded hits as a function of the activity in the previous bunch crossing, expressed as the scalar sum of transverse energy in all calorimeter clusters, ΣE_T. (b) The distribution of ΣE_T for unbiased events, where one unit corresponds to 24 MeV.
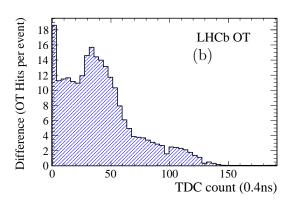
Figure 4: The recorded drift time spectrum for all hits in the Outer Tracker for no-bias events with 25 ns bunch spacing. (a) in blue, the same spectrum recorded while keeping only events with $\Sigma E_T(Prev) \leq 1000$. (b) the difference of the two TDC spectra, scaled such the difference is 0 at the $TDC = 150$ bin.

which contain a large fraction of spill-over hits from the previous bunch crossing. This is shown in figure 4(b) where the difference in TDC spectra before and after the cut is shown, normalized to the spectrum at TDC=150.

In addition to the early spill-over hits, also late hits from the current event are rejected, because the whole event is vetoed. These events can statistically be recovered with a looser threshold on the transverse energy of L0 hadron clusters. Effectively, the cut of events with a busy previous event will reduce the average OT event occupancy, less affected by spill-over contamination, allowing to increase the data-taking rate and speeding up the reconstruction processing time.

2.3   Hit asymmetries for both magnet polarities

The LHCb experiment is specialised in the study of *CP* asymmetries, and a crucial ingredient in these analyses are asymmetries in the detection of charged particles. To limit the impact from possible detector biases, the magnet polarity is regularly flipped during data taking.

From simulations it is known that more electrons than positrons are produced in secondary interactions with the detector material. The electrons are deflected in the so-called "down" polarity towards the negative x-direction (which corresponds to the so-called C-side in LHCb), and vice-versa for "up" polarity. This explains the asymmetric hit distribution in figure 5.

The two detector halves are not of equal width, and the split between the two halves is at $x = -8$ cm. As a result, the smaller width of the C-side registers less hits, which is compensated by the hits from the deflected negatively charged particles in the "down" polarity, leading to only 1.6% less hits in the C-side than in the A-side. For the "up"
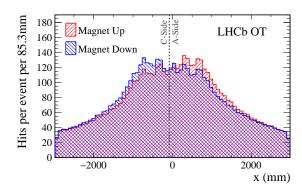
6

Figure 5: The hit distribution is shown for both magnet polarities, using 30,000 random events for both samples, without any trigger requirement. The vertical dashed line indicates the mechanical split between the two detector halves, at $x = -8$ cm.

polarity, the A-side registers 14.7% more hits than the C-side. The total number of hits, averaged for the two polarities, is equal for $x < 0$ compared to $x > 0$ within 0.4%.

2.4 Hit multiplicities in lead-lead and proton-lead collisions

The LHCb experiment has expanded its heavy-ion physics programme in Run 2, by recording PbPb collisions data in December 2015, and pPb and Pbp collisions data in November 2016. The relatively large OT straw diameter of 4.9 mm leads to a very large straw occupancy in PbPb collisions, preventing to reconstruct tracks of PbPb collisions at the largest centrality. The offline analysis is limited by the high occupancy in the whole LHCb detector to an event centrality smaller than 60%.

The OT occupancy for PbPb events is shown in figure 6, compared to the occupancy in nominal pp collisions, with an average pile-up of $\mu = 1.1$. The occupancy in pPb and Pbp collisions is also given, showing a slightly larger occupancy for the situation where the lead-ions are circulating in beam-1, i.e. in the direction of the LHCb spectrometer.
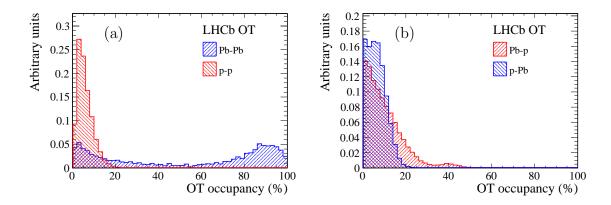
Figure 6: The average number of recorded hits (a) in minimum bias proton-proton and PbPb collisions and (b) pPb and Pbp collisions.

3 Mechanical stability

An alignment system was constructed to monitor the relative movements of the OT detector frames. The main purpose of the system is to confirm the mechanical stability of the detector. Any unforeseen movements of the detector components are monitored and can be used to confirm, or used as constraint for, the alignment procedure with reconstructed charged particle tracks [7, 8].
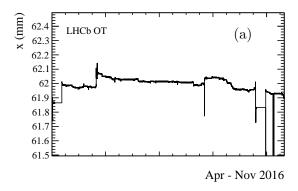
The system used for this purpose is called the Relative Alignment System of NIKHEF (RASNIK) [9]. A finely detailed image is projected through a lens onto a CCD camera. The light source is a 3×3 grid of infrared-emitting LEDs. These LEDs illuminate a coded mask. The mask consists of black-and-white squares in a chessboard-like pattern. The coded non-repeating pattern is used to obtain a unique position. The movement of the lens by a distance d in a direction perpendicular to the axis defined by the mask and the CCD camera causes a displacement of the image of the mask by a distance $2d$. The transverse position of the lens is then calculated from the image position by means of image processing of a CCD pixel frame. The image recorded by the CCD camera is then used to reconstruct positions of the chessboard pattern. The resolution of the CCD-RASNIK system is better than $1\,\mu\text{m}$ for a system with a mask-to-CCD distance up to about $8\,\text{m}$ [10].

Elements of 48 RASNIK lines are mounted on the four corners of each of the 12 C-frames of the OT detector. They measure precisely the x and y displacements of the four points on the C-frame with respect to corresponding fixed reference points, mounted on the bridge, the pillars or on the table fixed to the support structure. In addition to these 48 short horizontal lines, there are two longer vertical lines measuring displacements of the x and z coordinates of two positions on the top of the support bridge, with respect to the supporting table.

Below, the measured displacements are discussed regarding the long term stability, the reproducibility of the position after opening and closing a C-frame and the movements due changes of the magnet field of the LHCb dipole. All the misalignments here presented are automatically taken into account and corrected for via the LHCb software alignment [6].

3.1 Long term stability of C-frames positions

The horizontal lines measure the horizontal x and vertical y variations of positions of the points close to C-frames' corners. In figure 7(a) the movements along the x coordinate are shown, which is the coordinate relevant for the momentum measurement of charged particles. The RASNIK results show that the top parts of the C-frames are more stable in time than the bottom ones in both x and y coordinates. This is consistent with the mechanical constraints of the C-frames, which are fixed in x from the top of the bridge by means of a hook, clamped to the C-frames. The bottom of the C-frames are hanging freely in the x and y coordinates, while constrained in the z coordinate. The positions of the bottom C-frames vary within $\sim 200\,\mu\text{m}$ in both x and y values in 2016. At the beginning of the data taking, in May and June 2016, the changes are relatively large, in the range $100 - 200\,\mu\text{m}$. After an intervention at the end of June when parts of the
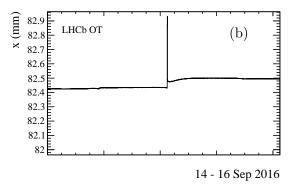
Figure 7: (a) Movements in x of one bottom corner of a C-frame (T2-XU) are shown during the data taking period in 2016. (b) Movement in x of a point at the top corner of an opened and closed C-frame (T3-VX, C-side) in September 2016. (The absolute value of the x-coordinate is arbitrary.)

detector were opened and closed, the OT slowly attained the equilibrium state. After a second intervention in September the OT reached its equilibrium in a shorter time. In October and November, the changes start to evolve with the opposite trend to the ones observed in May.

3.2   Effects of opening and closing C-frames

Two C-frames (x-u and v-x of the 3rd station – T3-XU and T3-VX – on the C-side) were opened and closed on 15th September 2016. The data from one day before and one day after the movement are presented in figure 7(b). The horizontal shift of about 70 μm in the x is observed due to the intervention. The vertical y coordinate changed by only 20 μm. It was also checked that the intervention on station T3 resulted in significantly smaller movements, within ±20 μm, of the other two stations that were not moved during the intervention. Changes in the weight distributions on the bridge during opening and closing C-frames, slightly affect all C-frames due to changing weight distributions of the bridge.

3.3   Monitoring of the bridge position

There are two lines which allow to measure the x and z LHCb coordinates of the points close to the top and on either side of the supporting bridge. The long term movement in z is shown in figure 8(a), whereas a zoom is shown in figure 8(b) in the period when the magnet was switched on and off several times. In May and June 2016, the bridge moves towards the magnet by about 100 μm and stabilizes in August and September. There is a hint that the trend reverses towards the end of the year and the z starts to increase. The sudden movements observed correspond to periods where the LHCb dipole magnet was switched off and on. The long term movement of the order 100 μm in the z direction is

10

small, and is presumably due to the combination of temperature variation and magnetic forces.
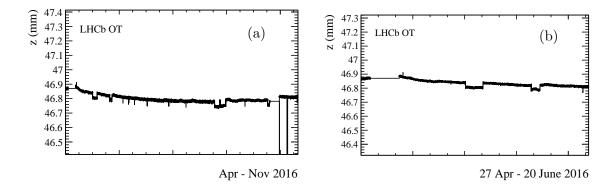

Figure 8: The z–coordinate of the bridge positions as a function of time (a) for the data acquired in 2016 and (b) the more detailed view of the data from 27th of April till 20th of June. The two visible dips correspond to the two occasions where the magnet was switched off and on.

The switching off of the magnet causes the movements of the bridge. After switching on the magnet, the bridge moves back to the previous position. The bridge position does not depend on the direction of magnet polarity.

In conclusion, the RASNIK system works well and provides high accuracy data which allows to monitor deformations of the OT detector geometry. The movements of the C-frames in the x and y coordinates are smaller than $200\,\mu m$. The movements of the bridge in the z direction with respect to the supporting table are within $100\,\mu m$. The results show small movements of the OT due to changes of magnetic field configurations and mechanical interventions, like opening and closing of C-frames. The RASNIK lines confirm the software alignment with precision data and show the real movements of the detector.

4 Radiation resistance

During the production of the OT detector modules, significant gain losses were measured after irradiation with ^{90}Sr or ^{55}Fe sources. This effect was studied extensively, and the origin was traced to the plastifier di-isopropyl-naphthalene used in the glue, which forms an insulating layer on the anode wire [11, 12]. After local irradiation, surprisingly the most affected region is upstream of the source with respect to the gas flow. Downstream the source, the deposition of the insulating layer is prevented by the presence of ozone, produced under the source. The irradiation profile on the OT surface during LHC operation is very different from the one of a small source in the laboratory, resulting in the fact that the entire OT benefits from the ozone production, and thus does not suffer from malicious depositions of an insulating layer of hydro-carbons on the anode wire. Nevertheless the

gain is monitored regularly during operation, to detect possible irradiation damage at the earliest stage.

To determine any change of the gain, dedicated data are recorded during LHC operation in which the amplifier threshold is varied per layer. To limit the impact on physics data taking, typically the low intensity fills from the LHC are used. However, the LHC conditions during these OT threshold scans can vary. These varying beam conditions lead to different event occupancies in the Outer Tracker. This was traced to be the origin of the small reported increase of the gain in the Outer Tracker in 2012, which was falsely attributed to a change in the gas mixture [13].
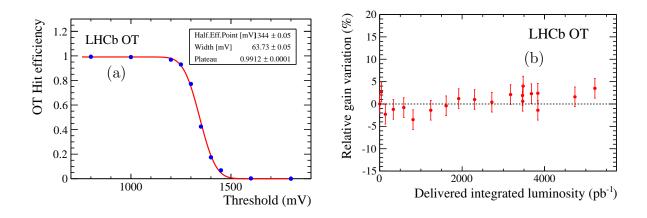

Figure 9: (a) Example hit efficiency plot as a function of amplifier threshold for the first layer. (b) Average gain variation as a function of the delivered luminosity.

The measured average gas gain with the nominal operational conditions is 55 000 and the charge deposited per single hit is of 350 fC. The typical hit density corresponds to about 2.8×10^{-3} per event per cm per straw in the innermost part, which is the one with highest multiplicity. For the considered time period a delivered luminosity of $5.2 \, \mathrm{fb}^{-1}$ was integrated for an equivalent charge of $0.18 \, \mathrm{C/cm}$ per straw.

Data from all the threshold scans have been re-analysed. To equalise the occupancy for each scan, an upper limit on the number of OT hits per event is placed offline. The single hit efficiency is computed in bins of the threshold value, which gives rise to the characteristic S-shape as shown in figure 9(a). The relative gain is then computed from the change in the half-efficiency point [13]. The relative gain throughout the years averaged over the full detector is shown in figure 9(b) as a function of the integrated luminosity. The results are consistent with no gain loss. The inner, outer and bottom parts of the detector are analysed separately as well, motivated by the originally observed ageing pattern upstream of the irradiated area. No differences are observed for the different regions of the detector. Within the resolution of the method (approximately $34 \times 34 \, \mathrm{cm}^2$) no large gain variations are seen in localized parts of the detector or in single straws.

Part II
Improved calibration and results

In this second part the improvements implemented during the long-shutdown are presented and evaluated. Prospects for future use of the added information are discussed.

5   Real-time global drift time calibration

The monitoring of the precise time alignment of the LHCb detector with respect to the LHC clock partially relies on the OT detector. The calibration of the time-alignment was performed in Run 1 only at given time intervals, typically after periods of shutdown with hardware interventions (technical stops). In order to increase the precision and automation of the OT time-alignment a procedure has been devised to perform this task online during data-taking time, and is described in the following.

5.1   Method

The OT measures the arrival time of the signals with respect to the LHC clock, T_{clk}, and is referred to as the TDC time, t_{TDC}. From the measurement of the distance r of a track traversing the straw to the wire at the centre of the straw, the expected time, $t(r)$ can be calculated using the distance to drift-time relation (TR-relation, see also section 7).

Different contributions can be distinguished in the TDC timing: the time-of-flight of the particle, t_{tof}, the drift-time t_{drift} of the electrons in the straw, the propagation time of the signal along the wire to the readout electronics, t_{prop}, and the delay induced by the FE electronics, t_{FE}, as shown in figure 10.

$$t_{\text{TDC}} = (T_{\text{collision}} - T_{\text{clk}}^{\text{FE}}) + t_{\text{tof}} + t_{\text{drift}} + t_{\text{prop}} + t_{\text{FE}} \quad (1)$$

The bunch crossing time of the pp collision, $T_{\text{collision}}$, can be shifted with respect to the LHC clock, T_{clk}, but the difference is kept below 0.5 ns. The phase of the clock used by the OT electronics at the TDC input (T_{clk}^{FE}) can be adjusted. The sum $(T_{\text{collision}} - T_{\text{clk}}^{\text{FE}}) + t_{\text{FE}}$ can be written as $(T_{\text{collision}} - T_{\text{clk}}) + t_0$, where the first difference accounts for variations of the phase of the LHC clock received at the LHCb experiment, and

Figure 10: Sketch of the contributions to the measured t_{TDC}.
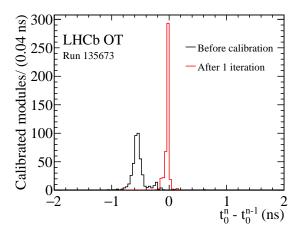
Figure 11: Example distribution of the differences between the t_0 values before and after the first iteration of the calibration (black), and between the first and the second iteration (red).

the $t_0 = t_{\mathrm{FE}} - t_{\mathrm{clk}}^{\mathrm{FE}}$ offset accounts for the drift of the global LHCb clock and the drift of FE electronic delays.

The TR-relation is calibrated on data (see section 7) and the time $t(r)$ obtained includes the effects of t_{tof}, t_{drift} and t_{prop}. The measured difference between $t(r)$ and t_{TDC} is fitted with a Gaussian distributions, which mean value determines the offset t_0.

During Run 1, the t_0 calibration was executed after every LHCb Technical Stop and the t_0 offset for each OT module was determined from the drift time residual distributions [5]. One iteration of the calibration procedure was sufficient to obtain the new t_0 values with a precision better than 0.1 ns. The distributions of the differences between the t_0 values before calibration and after the first iteration, and between the first and the second iteration are shown in figure 11. The largest contribution is due to a global t_0 shift that affects the t_0 constants of all FE modules by the same amount. This is caused by the drift of the global LHCb clock with respect to the bunch arrival time.

During Run 2, the t_0 calibration procedure is therefore split in two algorithms. The real-time algorithm performs a gaussian fit to the global drift time residual distribution considering the tracks in the whole Outer Tracker, estimating the impact of the drift of the LHCb clock. In addition, an offline algorithm is set up to evaluate the time offsets per OT module due to the single FE electronic delays. These latter offsets are not expected to change during the data-taking period, excluding cases of hardware interventions on the OT modules. This second algorithm has been used to calculate the offsets at the beginning of Run 2 and is then only used to confirm the stability of the t_0 constants (see section 6.2).

5.2 Performance and monitoring

The real-time global t_0 calibration strategy allows for a time alignment of the OT time and LHCb clock better than 0.1 ns, compared to global shifts of ± 0.5 ns which were allowed in Run 1. This leads to an increase of the track reconstruction efficiency by 0.25% with

14

respect to the previous calibration strategy. The track reconstruction efficiency has been estimated from a sample of simulated $B^+ \to J/\psi K^+$ decays reconstructed in the LHCb detector. The efficiency of tracks reconstructed in the whole LHCb tracking system, using the t_0 values included in the LHCb detector simulation, is compared to the tracking efficiency measured when varying the simulation t_0 offset by a global shift.

The real-time calibration algorithm uses the drift time residuals distributions obtained for the tracks reconstructed in the three OT stations to measure the current drift time offset (t_0 value) with respect to the t_0 value calculated from the previous calibration. This calibration is used in the online database during data taking. This calibration algorithm produces a fit to the global drift time residuals distribution every 15 minutes during physics data taking. The new t_0 value is applied if the following conditions are met: sufficient tracks were used in the new calibration; no t_0 calibration had been performed yet on the current run; the new t_0 value change exceeds 0.1 ns but is smaller than 2 ns.

The difference between the new t_0 value with respect to the previous t_0 value is reported in figure 12. The shadowed regions correspond to the minimum size of this difference necessary to trigger an update of the t_0 constants in the databases used for the data taking. The threshold value of 0.1 ns is considered optimal. It is the typical spread of the t_0 values per module after one or more calibration iterations, and thus implies a natural choice for the intrinsic resolution. Typically a few updates of the global t_0 constant are applied in one week of data taking.

The absolute t_0 as a function of time is shown in figure 13, together with the absolute value of the phase of beam-1. Any change in the LHC clock affects both measurements. The difference of the two measurements is shown in the lower figure of figure 13, and is
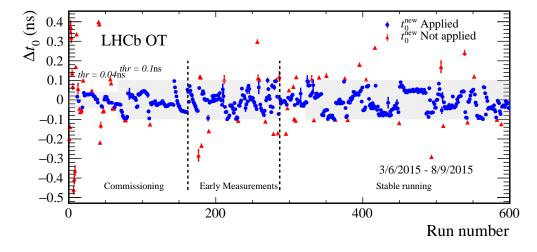

Figure 12: Calculated global drift-time offset differences (Δt_0) for Run 2 data taking period 3 July 2015 - 14 Sept 2015. Red triangles show calibrations above threshold which are applied to data, while blue dots show calibrations which are within tolerance and are not applied. The threshold values used are represented with the shaded region: the periods with lower threshold were during commissioning of this algorithm.
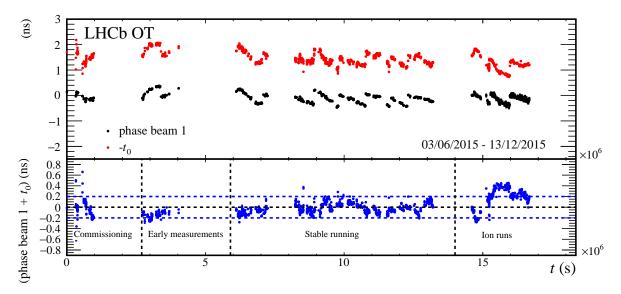
15

Figure 13: Absolute stability of the value of the global time offset t_0 obtained comparing the t_0 absolute value with the beam-1 phase. The large scatter in the initial points is due to the phase of commissioning of the algorithm. The t_0 measurements towards the end of the 2015 data taking period correspond to the LHC operation with Pb ions.

stable within ± 0.2 ns, showing the stability of the average OT time measurement. The large scatter in the initial points is due to the phase of commissioning of the algorithm. The larger differences > 0.2 ns in the last data taking period correspond to the data recorded during Pb running period at the end of 2015. Due to the larger number of low momentum tracks, the average time-of-flight difference is reflected in a different global t_0.

6 Offline per-module calibration

Time offsets due to small differences in the delays in single Front-End modules need to be accounted for, in addition to the global t_0 offset. These FE-offsets are not expected to change as function of time, unless in cases of hardware modifications of the system. Every FE module of the OT contains two layers of 64 straws, read out in groups of 32 channels, corresponding to one TDC chip per group. Two changes in Run 2 improve the time calibration of the OT module.

First, the calibration procedure assumes that the spatial position and alignment of the OT is correct. Since the calibration exploits the tracks and compares the measured time t_{TDC} to the time calculated from the measured distance from the track to the wire, $t(r)$, an imperfect spatial alignment of the detector will result in a systematic overestimation or underestimation of $t(r)$. The relative position of the two monolayers of straws inside a single module has been determined and accounted for in Run 2.

Secondly, the four different TDC chips within the same module measure different t_{TDC}

16

values, due to the slightly different characteristics. The t_{TDC} value measured can vary up to 1 ns within the same module. In Run 2 the granularity of the t_0 constants has been increased by a factor four, by determining the constant per TDC-chip, rather than per FE-module.

6.1 Module and monolayer spatial alignment

A major improvement of the alignment of the detector modules in Run 2 is provided by the real-time spatial alignment strategy [6]. At the beginning of each fill, a full tracker alignment is performed, and when the constants describing the position of the module differ from the last constants by more than a given threshold, the constants are updated. This ensures to have the OT modules aligned to better than $100\,\mu$m at all times.

Not only the alignment constants are updated more frequently, also the detector geometry description is improved. More parameters are introduced to describe the shape of a detector module. The OT half-module geometry is now modelled as a collection of 3 straight segments with equal length [5]. The numbers that parametrize the misalignment of the two monolayers are stored in the condition database. There are at most six numbers for each module. These six numbers represent the displacement in the x-coordinate between the two monolayers at the beginning and end of each of the three trajectory segments. In order to perform this special alignment, data from Run-I has been used. This new description of the detector elements leads to a reduction of the width of the drift time residuals distributions by up to 20% (See section 7) and a marginal increase of the number of reconstructed tracks and OT hits. The monolayer alignment is shown to be stable and is not updated online, but is monitored offline during Run 2.

6.2 FE-module t_0 calibration

The t_0 offsets for single TDC chips are calculated with respect to the global t_0 offset. This calibration is only run periodically as no relative movements of the modules are expected. For each module the drift time residual distributions are drawn for each TDC chip separately for tracks traversing the straws from the left and right side. A gaussian fit excluding the tails of the distributions is performed to determine the position of the drift time residuals peak. An arithmetic average between the t_0 obtained from left and right tracks is considered, and a t_0 value for each constant is determined and reported in the databases.

Different selection studies have been performed, including different requirements on the minimum numbers of OT hits and different lower limits on the momentum of the tracks. A tighter selection ensures a better quality of the track sample, but reduces the statistics. A compromise between the acceptable statistical uncertainty and track quality requirements is reached when using tracks traversing the whole LHCb tracking system, requiring an unbiased track-fit $\chi^2/\text{ndf} < 2$ and a minimum momentum of the particle of $3.2\,\text{GeV}/c$, which are standard requirements in typical LHCb physics analyses.

The gain in tracking efficiency obtained using per-TDC-chip t_0 constants rather than per-module constants has been estimated with simulated $B^+ \rightarrow J/\psi K^+$ decays reconstructed in the LHCb detector. The tracking efficiency improved marginally by about 0.5 per mille per track. The improvement in drift-time resolution and the corresponding possible new use of the time information are discussed below.

7 Updated drift-time distance relation and improved resolution

7.1 TR-relation

The drift-time measured by the detector needs to be converted to a distance from the wire to be used in the tracking. Drift-time and position information are related by means of the drift-time-distance relation, or TR-relation. The TR-relation is calibrated on data using good quality tracks, selected by requiring a momentum larger than $10\,\mathrm{GeV}/c$ and a track-fit $\chi^2/\mathrm{ndf} < 2$; the track-fit is unbiased by excluding the hit under study. The parametrization of the TR-relation is extracted from the fit to the distribution of the measured drift-time versus the distance of the reconstructed track from the wire, and is shown in figure 14. The TR-relation is parametrised with a second order polynomial as a function of the unbiased distance. The TR-relation with parameter values obtained with Run 2 data is

$$t(r) = \left(21.3\frac{|r|}{R} + 14.4\frac{|r|^2}{R^2}\right)\,\mathrm{ns},\tag{2}$$

where r is the distance and R is the radius of the straw-tube. The parameter values are consistent with the values observed in Run 1 [5].
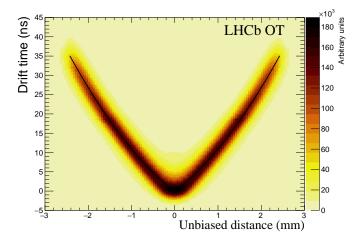

Figure 14: The drift time versus the unbiased distance distribution with the overlaid TR-relation curve, obtained from the fit (black line).

7.2 Resolution

The time resolution dependence on the distance from the wire is extracted from the 2-dimensional fit to the distribution in figure 14 to be

$$\sigma_t(r) = \left(2.25 + 0.3\frac{|r|}{R}\right) \text{ ns} \quad . \tag{3}$$

The average drift-time resolution is obtained from equation 3 to be 2.40 ns, which is an improvement of about 20% with respect to during Run 1. Similarly, the spatial resolution is reduced from 205 μm to 171 μm due to the combination of monolayer alignment, global drift time calibration and single FE-module calibration, discussed in the previous sections. The time and spatial distribution comparing the measured drift-time and hit position

Figure 15: (a) Drift-time residual distribution and (b) hit distance residual distribution.

of Run 1 and Run 2 are shown in figure 15 for illustration only, corrected for the finite precision of the track parameters.

8 Use of time information

The more precise time and space alignment, has led to an improved drift-time hit resolution of the OT, beyond its design specifications. This opens the possibility that timing information is assigned to physics objects, like reconstructed tracks and vertices. A sample of 100 000 selected events containing a semileptonic B meson decay has been used for this study.

8.1 Time-stamp for single tracks

A single track that traverses the entire OT typically contains 22 OT hits. For each hit the drift time residuals can be calculated, as described in section 5. The track time is defined as the sum of all individual drift time residuals, weighted by their errors. This track time is the difference in the arrival time of the particle at the OT with respect to the expected arrival time for a particle travelling at the speed of light. The number of OT hits per track used for the track time calculation is shown in figure 16(a). The mean number of hits is about 18, with a long tail to the left. The actual number of OT hits on a track is slightly larger, due to the addition of OT hits where the drift time is not used (for example for straws that are hit twice, and for which the drift time does not agree with the track position). Tracks with a number of hits less than three are not considered in these studies, and neither are tracks with a momentum below 2 GeV/c. The uncertainty of the track time is obtained from the drift time residual, σ_t, and is thus expected to scale as $\sigma_t/\sqrt{N}$, where N is the number of hits for the given track. The distribution is shown in figure 16(b), and has a mean value of 0.57 ns.

A track reconstructed with random OT hits (e.g. from noise or spill-over) is called a ghost track. The track time of ghost tracks is expected to be large, and could thus be of added value in their rejection. Studies on data show that the track time of ghost tracks
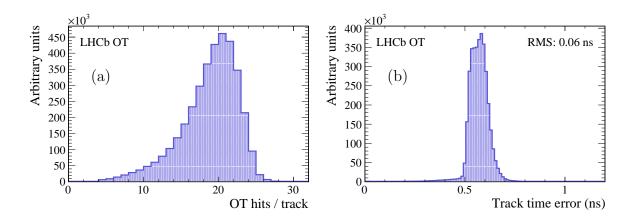

Figure 16: (a) The number of OT hits per track N, where the drift-time is used. (b) The uncertainty on the time per track, as estimated from time resolution per hit, $\sigma_t/\sqrt{N}$.

has indeed discriminating power, however it was also found that it is largely correlated with other ghost-reducing parameters, such as the χ^2 of the track fit, and thus adds little value.

8.2 Time-of-flight for pions and protons

The velocity of particles created in pp collision can mostly be approximated by the speed of light. However, heavy, low momentum particles have a lower velocity, which can lead to a significant later arrival time. For protons, this is about $0.5\,\text{ns}$ at $5\,\text{GeV}/c$ at the centre of the OT - about $8.5\,\text{m}$ from the interaction point - as shown in figure 17. This is similar to the expected track time resolution.

The distribution of track times of pions and protons with momenta below 7 GeV/c in LHCb simulation is shown in figure 18(a). In data, a sample of D^* tagged $D^0 \to K^+\pi^-$ decays is used as a source of unbiased identified pions. This sample is regularly used to calibrate the LHCb particle identification response, since pions can be identified using only their charge. In a similar fashion, events with a semileptonic Λ_b^0 decay are used as a control sample of protons, albeit that the initial selection discards a large fraction of low-momentum protons. The track time distribution in data is shown for both pions and protons in figure 18(b). In both simulation and data the difference in the track time distributions between low momentum pions and protons is clearly visible. The discriminating power of the track time to distinguish protons from pions is shown in figure 19. The performance in data and simulation are found to be in good agreement. As an example, for a proton identification efficiency around 75%, half of the pions are
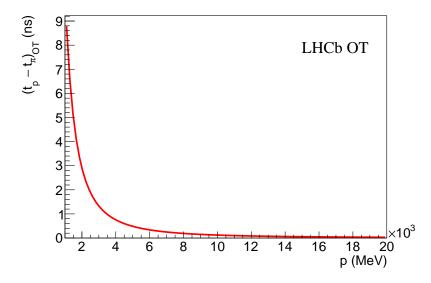

Figure 17: The difference in time-of-flight between protons and pions as a function of their momentum.
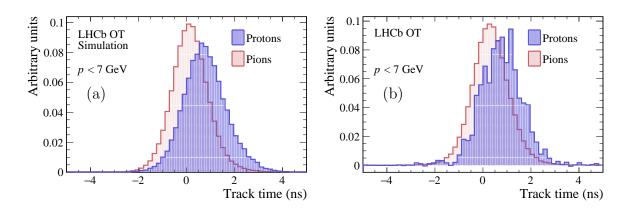
21

rejected.

Figure 18: The distribution of track times for protons and pions with $p < 7\,\text{GeV}/c$ in (a) simulation and (b) in data.
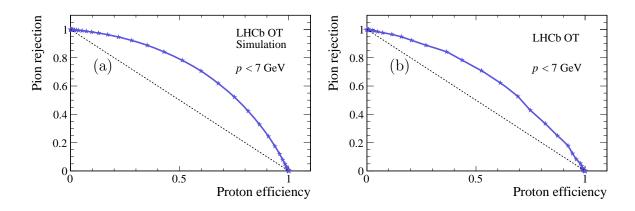

Figure 19: The pion rejection rate as a function of the proton efficiency for (a) simulation and (b) data.

Most of the particle identification performance of LHCb is due to the ring imaging Cherenkov detectors (RICH), with radiators CF_4 and C_4F_{10}. The particle identification for momenta between 1.5 and $10\,\text{GeV}/c$ was done with the use of the aerogel radiator, but it has been removed after Run 1 fitting the design for higher luminosities. The OT track time can assist in this momentum range in Run 2, especially for analyses involving protons, Σ hyperons, deuterons, and new long-lived heavy particle searches. In LHCb, particle identification is done by creating a neural network using inputs from the RICH, calorimeters and muon detector systems [14]. In the near future the OT track time will be added as an input variable. The addition of the OT track-time will improve also the performance of particle identification of low-momentum particles used to identify the

flavour of B-mesons (flavour tagging). Finally, the particle identification performance of the OT track time serves as a test case for a possible future time-of-flight detectors for LHC, such as for example TORCH [15].

8.3   Time-stamp of primary vertices

One of the experimental limitations to increase the luminosity at LHCb is the number of pp collisions per bunch crossing, which hampers the association of a B-decay to the correct primary vertex. Two primary vertices (PVs) separated far enough in space can be resolved by the excellent spatial resolution of the vertex reconstruction. A time stamp per PV would aid in the separation of these vertices. The PV time is calculated as the weighted average of the track times of all tracks associated with that PV. For events with two PVs, the PV time difference is shown in figure 20(a). The expected error for this spread is $\sigma_{t,track}/\sqrt{N_{tracks}}$, where N_{tracks} is the number of tracks per PV, which is 25 on average. The significance of this spread when comparing to the expected error is found to be larger than one, indicating some discriminating power. However, it is also larger than the combined expected PV time uncertainty $(0.57\,\text{ns}/\sqrt{25})$ with the PV spread of $0.18\,\text{ns}$ that is expected from the LHC [16].
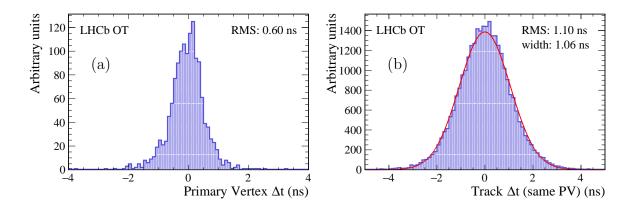

Figure 20: (a) The difference between the average time per primary vertex, for events with two reconstructed primary vertices. (b) The difference between the time of two tracks belonging to the same primary vertex.

In figure 20(b) the difference in track time between two tracks from the same PV is shown. The RMS is larger than the expected value of $0.57 \times \sqrt{2}\,\text{ns}$. This indicates that the track time errors are underestimated by about 20%.

9   Conclusions

In this article the performance of the LHCb Outer Tracker detector has been summarized as obtained from LHC Run 2 data.

The OT has reached and in some cases superseded the design performances, being able to acquire data in pp collisions at luminosities twice higher than anticipated and to be run in the high multiplicity environment of heavy ion collisions.

Efficiencies and availability of the detector components have been kept at maximal level for the entire data taking period, and no signs of ageing or damages due to radiation have been observed.

Novel methods have been implemented for the time and space alignment, which have improved the resolution of the detector. This allowed the study to apply the time information beyond the tracking purposes. A time-of-flight measurement has been developed providing discrimination for particle identification of low momentum charged hadrons, and that will be helpful in physics analyses with Run 2 data. This offers also benchmarking possibilities for future time-sensitive detectors for particle identification or multiple-interactions event tagging.

Acknowledgements

References

[1] LHCb collaboration, A. A. Alves Jr. *et al.*, *The LHCb detector at the LHC*, JINST **3** (2008) S08005.

[2] LHCb collaboration, P. R. Barbosa *et al.*, *Outer Tracker technical design report*, CERN-LHCC-2001-024.

[3] A. Berkien *et al.*, *The LHCb Outer Tracker front end electronics*, CERN-LHCB-2005-025.

[4] G. Haefeli *et al.*, *The LHCb DAQ interface board TELL1*, Nucl. Instrum. Meth. **A560** (2006) 494.

[5] LHCb Outer Tracker group, Arink *et al.*, *Performance of the LHCb Outer Tracker*, J. Instrum. **9** (2013) P01002. 30 p, `arXiv:1311.3893`.

[6] S. Borghi, *Novel real-time alignment and calibration of the lhcb detector and its performance*, Nucl. Instrum. Meth. **A845** (2017) 560 , Proceedings of the Vienna Conference on Instrumentation 2016.

[7] W. Hulsbergen, *The global covariance matrix of tracks fitted with a Kalman filter and an application in detector alignment*, Nucl. Instrum. Meth. **A600** (2009) 471, `arXiv:0810.2241`.

[8] J. Amoraal *et al.*, *Application of vertex and mass constraints in track-based alignment*, Nucl. Instrum. Meth. **A712** (2013) 48, `arXiv:1207.4756`.

[9] P. Duinker *et al.*, *Some Methods and Tools for Testing and Optimizing Proportional Wire Chambers*, Nucl. Instrum. Meth. **A273** (1988) 814; M. Adamus *et al.*, *Test results of the RASNIK optical alignment monitoring system for the LHCb Outer Tracker Detector*, LHCb-Note-2001-004; M. Adamus *et al.*, *First Results from a prototype of the RASNIK alignment system for the Outer Tracker detector in LHCb experiment*, LHCb-Note-2002-016.

[10] H. Dekker *et al.*, *The RASNIK/CCD 3-dimensional alignment system*, eConf **C930928** (1993) 017, ATL-MUON-94-063.

[11] S. Bachmann *et al.*, *Ageing in the LHCb Outer Tracker: phenomenon, culprit and effect of oxygen*, Nucl. Instrum. Meth. **A617** (2010) 202.

[12] N. Tuning *et al.*, *Ageing in the LHCb outer tracker: aromatic hydrocarbons and wire cleaning*, Nucl. Instrum. Meth. **A656** (2011) 45.

[13] D. van Eijk *et al.*, *Radiation hardness of the LHCb Outer Tracker*, Nucl. Instrum. Meth. **A685** (2012) 62.

[14] L. Anderlini *et al.*, *The PIDCalib package*, Tech. Rep. LHCb-PUB-2016-021. CERN-LHCb-PUB-2016-021, CERN, Geneva, Jul, 2016.

[15] M. J. Charles and R. Forty, *TORCH: Time of Flight Identification with Cherenkov Radiation*, Nucl. Instrum. Meth. **A639** (2011) 173, `arXiv:1009.3793`.

[16] G. Arduini, *private communication*, 2016.